Reduced graphene oxide-based broad band photodetector and temperature sensor: effect of gas adsorption on optoelectrical properties

4 authors, including:

Mustaque A Khan
Indian Institute of Science
6 PUBLICATIONS **3** CITATIONS

Some of the authors of this publication are also working on these related projects:

Project   Photodetector View project

Project   Temperature sensor View project

Reduced Graphene Oxide Based Broad Band Photodetector and Temperature Sensor: Effect of Gas Adsorption on Opto-electrical Properties

Mustaque A. Khan,[†§]*Kishan L. Kumawat*,[† §]*Karuna K. Nanda*,[†]*Saluru B. Krupanidhi*[†]*

[†] Materials Research Centre, Indian Institute of Science, Bengaluru -560012, India

§ contributed equally, *Corresponding Author: sbkenator@gmail.com

Abstract

Reduced graphene oxide (rGO) has found tremendous application due to its versatile and tunable properties. We have prepared rGO by green hydrothermal method without using any toxic additives that comprise of ~ 5-14 layers with an average interlayer distance of 3.5 Å. Device with Ag-rGO-Ag configuration has been fabricated that exhibits excellent stable and reproducible photoresponse properties ranging from UV−VIS (ultraviolet-visible) to near IR (infrared) region. Responsivity and external quantum efficiency (EQE) values are as high as 0.71, 0.733, 0.230 and $0.313 A.W^{-1}$ and 57, 85, 88 and 120% using 1550, 1064, 632 and 325 nm wavelength, respectively. We have shown that the temperature-dependent resistance follows a well-definite exponential behavior which indicates potential application of rGO as temperature sensor. Overall, these results suggest that rGO can be a potential material for low-cost, environment-friendly and efficient broadband photodetector and temperature sensor. Also,

pressure-dependent opto-electrical measurements have been carried out that reveal adsorption characteristic of various gases.

Keywords: photodetector; temperature sensor; smart sensor, electrical transport; gas adsorption.

1. Introduction:

Photodetection in broad range of wavelength can be used for a wide range of opto-electronic and photonic applications, such as pollution detection, light communication interconnects, imaging, remote sensing, biomedical applications, etc (Arora et al., 2008, Degner et al., 2009, Burgard et al., 2006, Grobe et al., 2013, Dias et al., 2017b). Due to its' zero band gap and high carrier mobility graphene was expected to be a potential material for broadband ultrafast photodetector. However, due to poor absorption and fast recombination, responsivity of graphene photodetectors is as low as few mAW^{-1} or less (Nair et al., 2008, Chang et al., 2013, George et al., 2008). Plasmonic nanoparticles or microcavity has been used to increase sensitivity of graphene photodetector (Liu et al., 2011b, Furchi et al., 2012). Although these modifications have been shown some improvement, the enhanced sensitivity is limited to narrow spectrum range. In addition, processing and fabrication of graphene-based photodetectors are challenging and time consuming. On the other hand, due to easy scalable preparation method and tunable properties of its derivative, reduced graphene oxide (rGO) can be a low-cost effective alternative to graphene.

Chitara et al. obtained a responsivity of 0.12 AW^{-1} and 40 % EQE at 360 nm irradiation using rGO synthesized in DMF with toxic hydrazine mono hydrate (Chitara et al., 2011). Thermally reduced graphene oxide has been studied by Chowdhury et al, and Chang et al. (Chowdhury et al., 2014, Chang et al., 2013). Chowdhury et al. found a maximum responsivity of 0.55 $A.W^{-1}$ and

EQE of 57% at 2 V using IR bulb. Chang et al. achieved a responsivity of 0.7 A.W^{-1} with a high applied bias of 19 V. In most of these cases, photodetection studies were carried out with a radiation of specific wavelength or within a narrow range of electromagnetic radiation. Furthermore, bulb has been used for photodetection in many cases (Chowdhury et al., 2014, Kumar et al., 2014, Parikshit et al., 2016). As bulbs produce lots of heat, that itself can change the active material resistance causing error in the evaluation of the photoresponse properties of the materials.

Here, we have used a green hydrothermal reduction method (without any added chemicals) for reduction of graphene oxide (GO). rGO exhibits excellent broadband photoresponse and achieved responsivity better than many other reported values. We have also carried out temperature- dependent electrical measurements and analyzed carrier transport mechanism in rGO film. Resistance (R) is found to follow a well-defined exponential behavior, which indicates its potential application as a temperature sensor. Interestingly, the temperature coefficient of resistance (TCR) is superior to the many commercial temperature sensors. We have also studied gas pressure dependent opto-electrical properties of rGO. Resistance variation with pressure resembles its gas adsorption characteristic. These measurements pave the path for further improvement in responsivity in RGO based devices.

2. Experimental Methods:

Graphite flakes were purchased from Sigma-Aldrich. Potassium permanganate ($KMnO_4$), hydrochloric acid (HCl) and sulfuric acid (H_2SO_4) were purchased from Fisher Scientific. Ethanol was purchased from local supplier.

2.1 *Preparation of graphene oxide (GO):*

GO is prepared by modified Hammer's method (Hummers Jr and Offeman, 1958). In brief, graphite flakes (2g) and $NaNO_3$ (1g) are dissolved in 50 ml H_2SO_4 by stirring for half an hour in an ice bath. 6g $KMnO_4$ is added into the mixture slowly over the period of 20 minutes and stirred for 1 h. As-obtained solution mixture is then heated at 35°C with continuous stirring for 2 h. Then 80 ml of deionized water is added to the solution mixture and heated at 98°C for 15 minutes. The solution mixture is then diluted with 280 ml deionized water and 50 ml of 30% H_2O_2 solution. The final product is collected by filtering the solution followed by washing with 5% HCl solution, deionized water and drying at 50°C for 24 h.

2.2 *Synthesis of rGO:*

80 mg of GO is dissolved in 40 ml of water by sonication. The solution is transferred to Teflon-lined stainless-steel autoclave and heated at 180°C for 24 h in muffle furnace. The black color product which is obtained by centrifugation followed by washing with ethanol is dried in a vacuum desiccator.

2.3 *Structural characterization:*

The powder X-ray diffraction (XRD) patterns of GO and rGO have been taken by using Rigaku SmartLab X-ray diffractometer with Cu K_α source (wavelength = 1.5405 Å). The morphology of the rGO is determined by scanning electron microscope (SEM, Zeiss Gemini ultra55). Absorbance spectra have been acquired using PerkinElmer- Lambda 750 spectrophotometer in the wavelength range 200-800 nm. Interlayer distance of rGO is determined by transmission electron microscopy (TEM, Jeol JEM 2100F). Defects analysis has been carried out with Raman spectroscopy (LabRAM HR) using 532 nm laser excitation. Elemental composition is determined by X-ray photoelectronic spectrometer (XPS, AXIS ULTRA) and energy dispersive

spectroscopy (EDS, OXFORD INSTRUMENTS). Structural characterization results have been discussed in supplementary information (figures S1-S3).

2.4 *Device fabrication and optical characterization:*

rGO (4.5 mg) is dispersed in 150 µl toluene by ultrasonication and a film is made by drop casting the solution on 95 µm channel of a silver coated (200 nm thick) cleaned quartz glass (figure S4). Gas adsorption studies have been done with 1 mm wide channel of silver electrodes. Drop-casted film is dried on hot plate at 40°C for 45 min. Electrical contacts are made using copper wire and silver paste.

CNI's MDL-III 1550 nm (beam radius 2 mm) and MIL-III 1064 nm (beam radius 2.5 mm) lasers have been used as the IR source. Melles Griot 632 nm He-Ne (beam diameter 0.8 mm) and 325 nm He–Cd lasers (beam diameter 1.4 mm) have been used for visible and ultra-violet source, respectively. Electrical measurements have been carried out using Tektronix Keithley 2400 source with LabVIEW interface.

3. Results and Discussion:

3.1 *Photodetection properties of rGO:*

Photodetection properties of the rGO have been carried out from 1550 to 325 nm in electromagnetic spectrum. Figure 1a-d show the temporal photoresponse of rGO for 1550, 1064, 632 and 325 nm laser irradiation. These measurements show that photocurrent rises immediately as soon as light is shined and slowly saturates. Photocurrent increases with increasing light intensity. Variation of photocurrent with intensity has been plotted in figure 1e and fitted
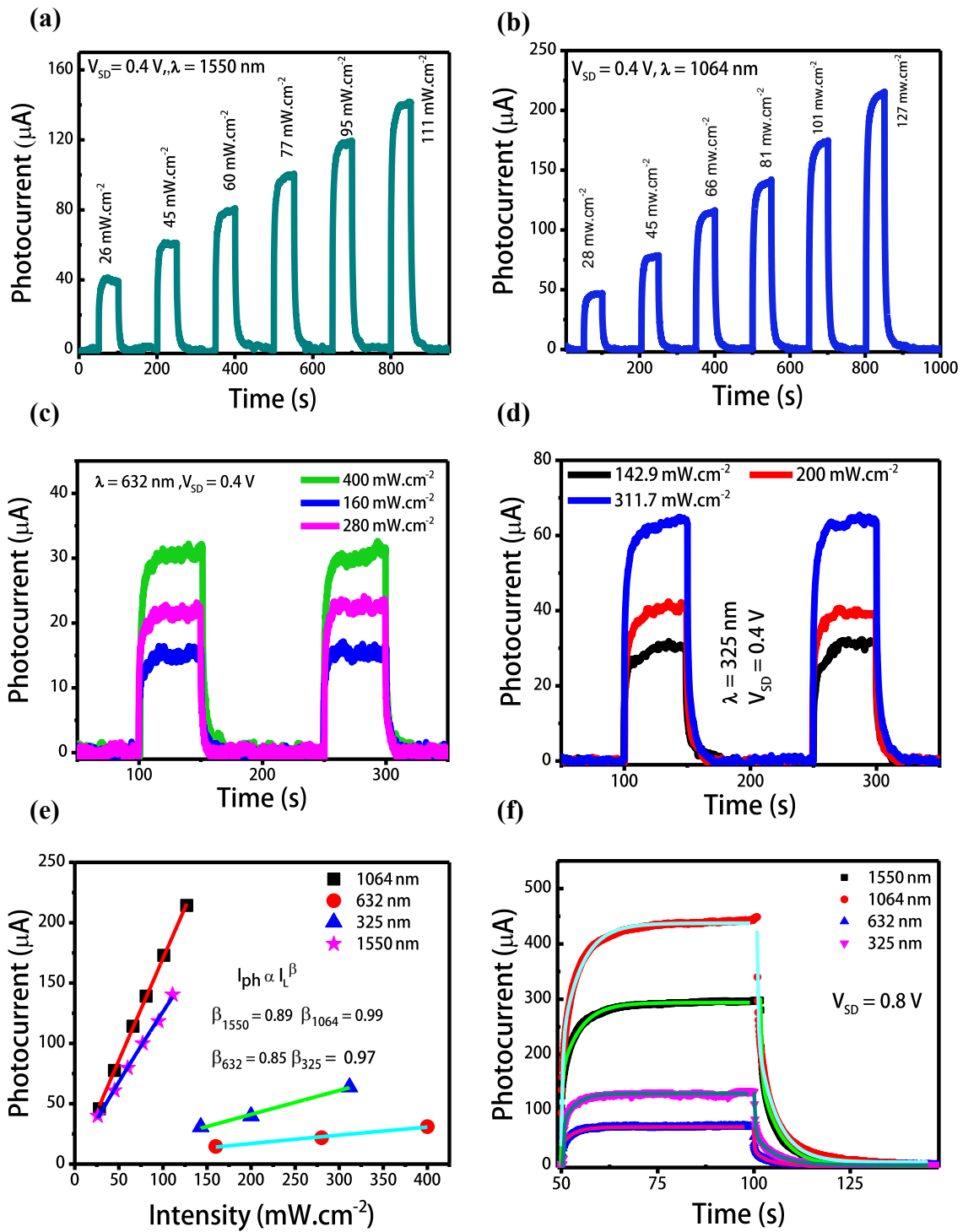
Figure 1: (a), (b), (c), (d) Temporal photoresponse at different intensities with 1550, 1064,632 and 325 nm respectively, (e) variation photocurrent with intensity, (f) rise and decay of photocurrent and their exponential fittings,

with the following equation,

$$I_{Ph} = \alpha * I_L^{\beta}$$

where α and β are constant (Mukhokosi et al., 2018, Khan et al., 2017a, Mallampati et al., 2015). β depends on complex processes of exciton generation, trapping, and recombination (Zhang et al., 2013, Kind et al., 2002). β is 0.89, 0.99, 0.85 and 0.97 for 1550, 1064, 632 and 325 nm wavelength respectively. β value of 1 suggest monomolecular recombination and β value 0.5 suggest bimolecular recombination. $0.5 < \beta < 1.0$ suggests presence of trap states in rGO (Kumar and Thangaraj, 2008). Temporal photoresponse with variation of bias for different incident light have been shown in figure S5 a-d and the photocurrent variation with bias has been plotted in figure S5 e. Variation with bias voltage shows excellent linear variation with R^2 (adjusted R-squared) value of 0.99 for all cases. Photodetector parameters like responsivity, EQE have been evaluated from the temporal response curves. Responsivity is defined as the photocurrent (I_{Ph}) generated per unit illumination intensity (I_L) per unit area (A),

$$R = I_{Ph}/(I_L \times A)$$

and EQE is determined as the number of electron generated per incident photon

$$EQE = hCR/(q \times \lambda)$$

where h is Plank constant 6.626×10^{-34} J.s., C is light speed 3×10^8 m.s^{-1}, q is electronic charge $(1.6 \times 10^{-19}$ coulomb) and λ is the wavelength of incident radiation (Khan et al., 2017b, Xia et al., 2009, Afzali et al., 2014). Responsivity and EQE of the device with other reported data at different incident electromagnetic radiation have been listed in table 1.

Also, rise and decay of photocurrent (figure 1f) has been fitted with the exponential equation

$$I_t = I_f + A_1 * exp[-(t - t_0)/\tau_1] + A_2 * exp[-(t - t_0)/\tau_2)] ,$$

where I_t is photocurrent at time t and I_f is the final photocurrent, τ_1, τ_2 are time constants and A_1 and A_2 are constants (Chang et al., 2013, Ito et al., 2016). Time constant values of the device at different incident electromagnetic radiation have been listed in table 1. Two-time constants for rise and decay indicate a faster rise (or decay) followed by slower saturation due to the effects of charge traps. Reproducibility of photocurrent over 10 cycles is shown in figure S 6.
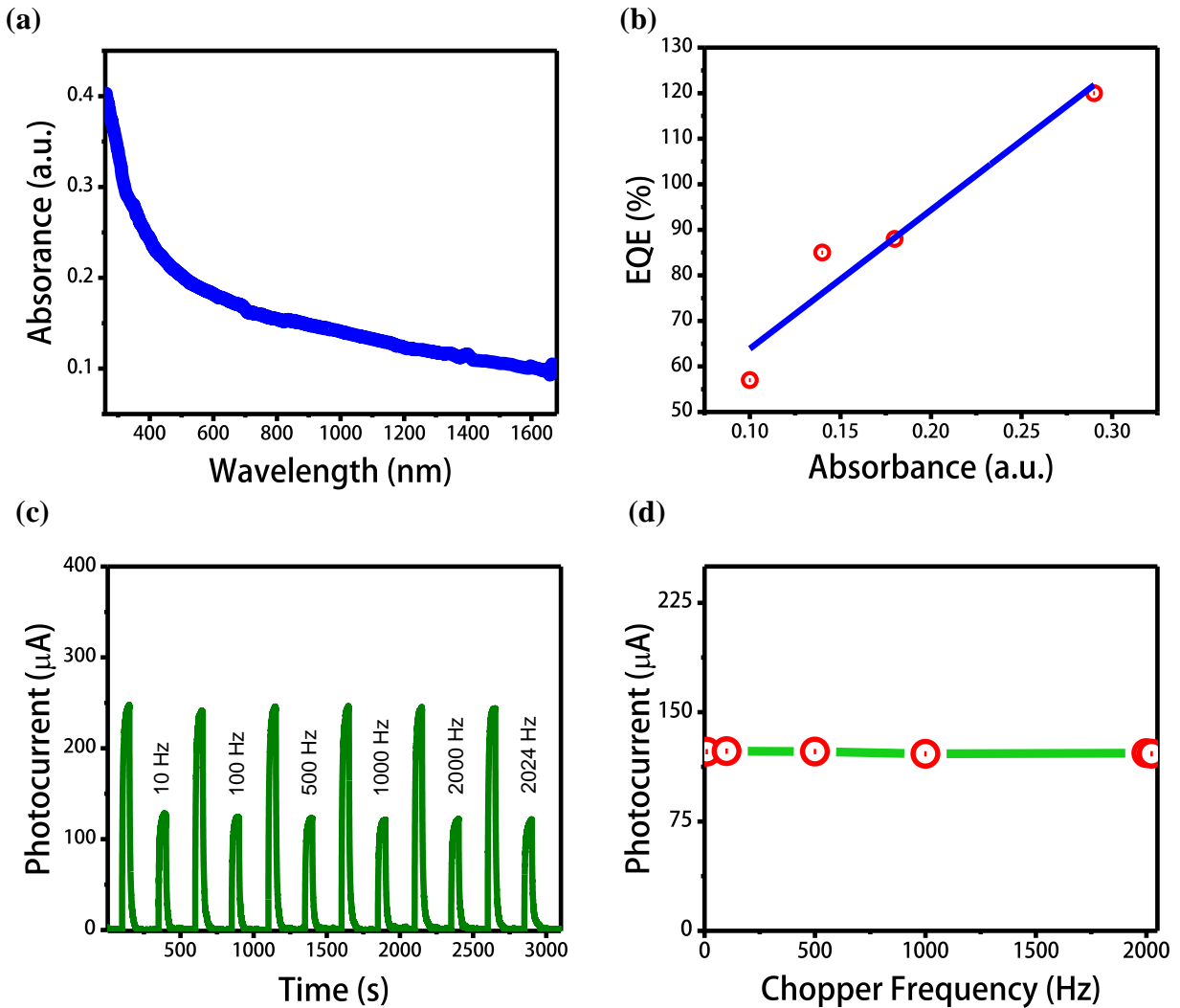

Figure 2: (a) absorbance of rGO vs. wavelength in NMP solution, (b) EQE vs. absorbance plot for Ag-rGO-Ag, (c) temporal photoresponse at different chopping frequency, (d) photocurrent vs. chopping frequency.

We have recorded absorbance spectra of rGO in N-Methyl-2-pyrrolidone and plotted EQE (%)

vs. absorbance at different wavelength (figure 2 a,b). EQE vs. absorbance plot has been fitted with linear equation and the fit has an adj. R-square value 0.902. Thus EQE increases almost linearly with light absorbance and at lower wavelength where the absorbance is higher EQE value even exceeds 100%.

When photocurrent is probed using bulb or IR lamp, a large amount of heat is produced that can cause change in resistance and hence, the photocurrent. Figure 2c shows temporal photoresponse at different chopping frequency. Variation of photocurrent in presence of chopper with a varying frequency of 10 to 2024 Hz has been shown in figure 2d. If photocurrent is due to heating of the active material which reduces the resistance (bolometric effect), it should decrease with increasing chopping frequency. While determining the photocurrent in our case, chopper blocks the path of the laser light for half time, hence, photocurrent gets reduced to half and it's stable with the chopper frequency. This result supports that there is no bolometric effect.

It may be noted that our RGO based device shows a superior performance over other device. First of all, ZnO, GaN, Ga_2O_3 and many other photodetectors work in a short spectrum of electromagnetic radiation and also rGO based photodetectors have been explored mostly either in IR or UV(/VIS) range. On the contrary, our rGO based photodetector has been studied over broadband and it shows efficient, stable and reproducible photodetection properties. Mostly graphene based photodetectors exhibit a responsivity in few ten of $mA.W^{-1}$ due to fast recombination of photogenerated carriers. Photodetection properties of rGO depend on C/O ratio, structural and impurity defects (Khan et al., 2017b). While increased reduction increases absorption in rGO (Li et al., 2008), defects in rGO can trap or scatter photogenerated carriers which can lead to longer life time of electrons and holes (Gowda et al., 2014).

Table 1: A short comparison of various characteristics of different photodetectors.

Active Material	λ (nm)	Bias (V)	Rise (s) τ_1	Rise (s) τ_2	Decay(s) τ_1	Decay(s) τ_2	R (A/W)	EQE (%)
RGO (Chang et al., 2013)	895	19	2	20	6	90	0.7	
Au/Graphene (Liu et al., 2011b)	514	$V_{SD} = 0$ $V_G = -20$					0.006	1.5
RGO (Chitara et al., 2011)	360	1	1800		2100		0.120	40
RGO (Chowdhury et al., 2014)	IR Lamp	2	240		300		0.55	57
Graphene (Xia et al., 2009)	1550	$V_G = 80$					0.0005	
G-QD (Zhang et al., 2015)	254	5					0.002	0.7
Cu-Ni / Graphene (Kumar et al., 2014)	White Light	5	0.84	31.73	2.22	93.19		
Cu_2SnS_3 (Dias and Krupanidhi, 2016, Dias et al., 2017a)	IR Lamp	3 0					0.016 0.007	2.53 1.19
Chip Integrated Graphene (Gan et al., 2013)	1450-1590	1					0.100	
Wrinkled Graphene (Gowda et al., 2014)	1550						12.5×10^{-6}	
RGO (This Work)	1550	0.8	0.15	4.47	0.41	5.37	0.71	57
	1064	0.8	0.37	5.11	0.29	5.19	0.733	85
	632	0.8	0.12	6.75	0.19	3.41	0.230	88
	325	0.8	0.23	3.35	0.26	5.28	0.313	120

These mechanisms can enhance responsivity by increasing carrier collection probability. C/O ratio of prepared rGO is ~6.45 and presence of defect is obvious from Raman spectrum of rGO (I_D/I_G ~ 2.43). Achieved responsivity and EQE in our rGO based device are quite high when compared to many other devices at similar experimental conditions.

3.2 *Electrical transport and temperature sensing*

Current vs. voltage measurement for rGO device has been carried out at different temperature and reported in figure 3a. We have systematically analyzed I-V characteristics to determine the transport in Ag-rGO-Ag film. In figure 3b, we have plotted ln(I) vs. ln(V) and a linear fit that produces a slope of 1 suggesting Ohmic conduction, characterized by the equation,

$$ \mathbf{I \propto V * exp\left[-\frac{\Delta E}{k_B T}\right]}, $$

where ΔE is the activation energy (Jung et al., 2011, Altuntas et al., 2015).

We have also tried to fit the I-V characteristics with other transport mechanisms such as Poole-Frenkel transport (figure S7 a). Fowler-Nordheim transport mechanism (figure S7 b), Schotky Emission (figure S7 c) and Trap Assisted Tunneling (figure S7 d) have also been examined. As none of these plots produce any straight line in any portion of the corresponding plots and hence, these transport mechanisms are excluded from possible transport mechanisms.

To determine the temperature dependence of carrier transport in figure 3c we have plotted ln(I) vs. T^{-x}. The best fitting straight line has been obtained with x =1 which indicates band gap excitation of carriers and suggests the minimum temperature used is enough to overcome the band gap of rGO (Muchharla et al., 2014).

Resistance (**R**) variation with temperature has been shown in figure 3d and fitted with exponential equation,

$$R = A_0 * exp\left[\frac{\Delta E}{k_B T}\right].$$

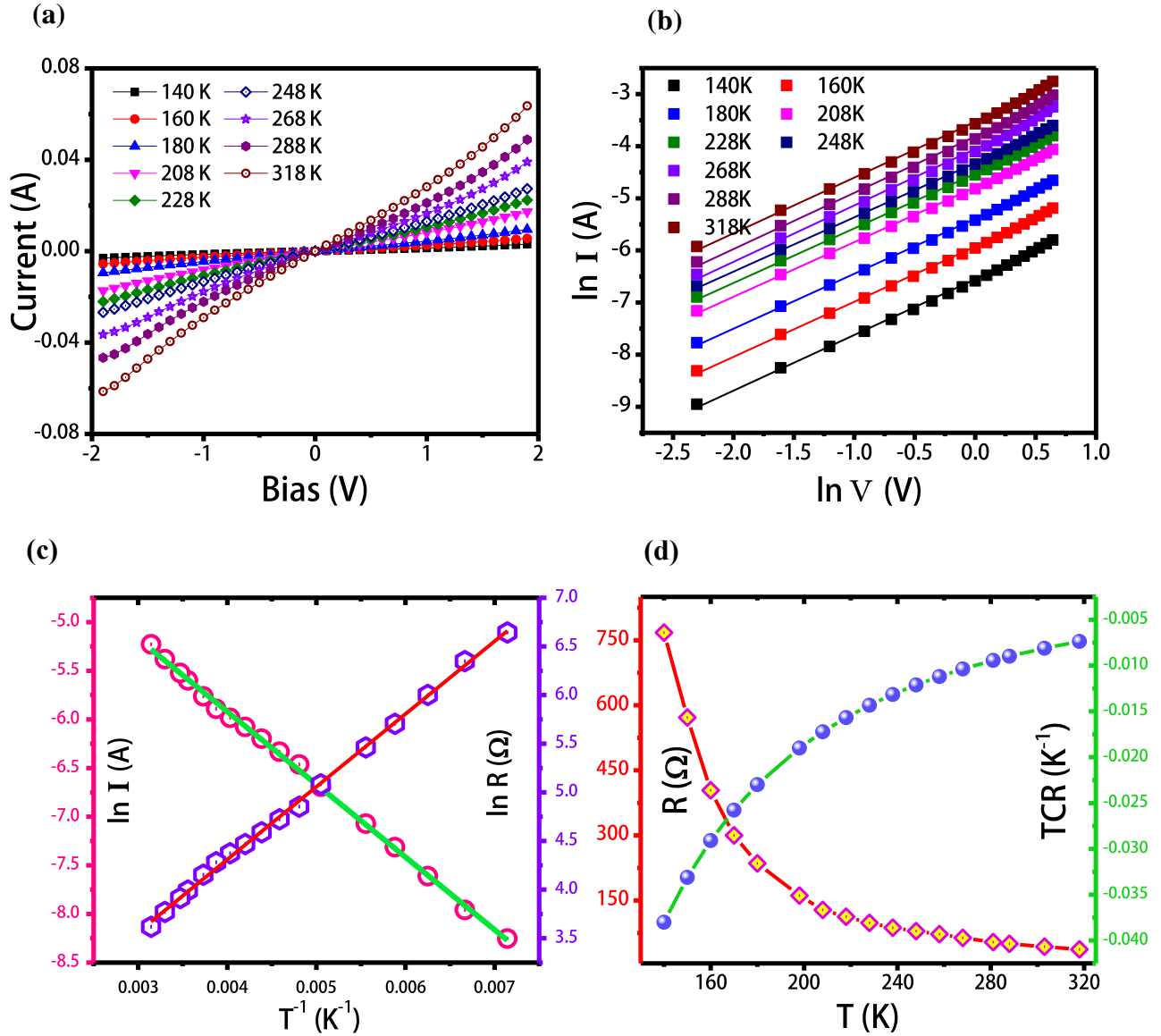**(a)**

(b)

(c)

(d)

Figure 3: (a) I-V characteristics at different temperatures, (b) ln(I) vs. ln(V) plot and linear fittings, (c) ln(I) and (R) vs. inverse of temperature (1/T), (d) R and TCR vs. temperature.

The value of the constant ΔE is $64.4*10^{-3}$ eV. As resistance of the device follows a defined equation, it can be exploited as a temperature sensor. Temperature coefficient of resistance (TCR) is defined as

$$TCR = \frac{1}{R}\frac{dR}{dT} \text{ , (Von Arx et al., 1997).}$$

Now if we use the expression of R in the above equation then

$$TCR = -\frac{\Delta E}{K_B T^2} \text{ .}$$

This equation is similar to the expression for relative sensitivity in fluorescence intensity ratio based optical temperature sensors (Senapati and Nanda, 2017). TCR values have been plotted in figure 3d and it varies from $-3.5*10^{-2}$ °C^{-1} and $-7.4*10^{-3}$ °C^{-1} in 140 K to 318 K temperature range. TCR of commercially available Pt based sensor is ~ $3.92*10^{-3}$°C^{-1} (Tsutsumi et al., 2002). Thus, sensitivity of the rGO as a temperature sensor is better as compared to commercially available ones.

3.3 *Pressure-dependent opto-electrical measurement*

During electrical measurement in vacuum we have observed change in resistance with variation of pressure, which lead us to investigate pressure-dependent opto-electrical properties. Figure 4 a,b show pressure dependent current (I) and change of resistance (ΔR with respect to resistance at zero pressure) correspondingly in nitrogen and argon atmosphere. Current (I) value decreases and ΔR increases with increasing gas pressure and almost saturates after certain pressure (figure 4 a,b). Similar observations have been made in case of oxygen and air (figure S8 a,b) as well. ΔR value is proportional to the amount of gas adsorbed. ΔR values have been fitted with the equations
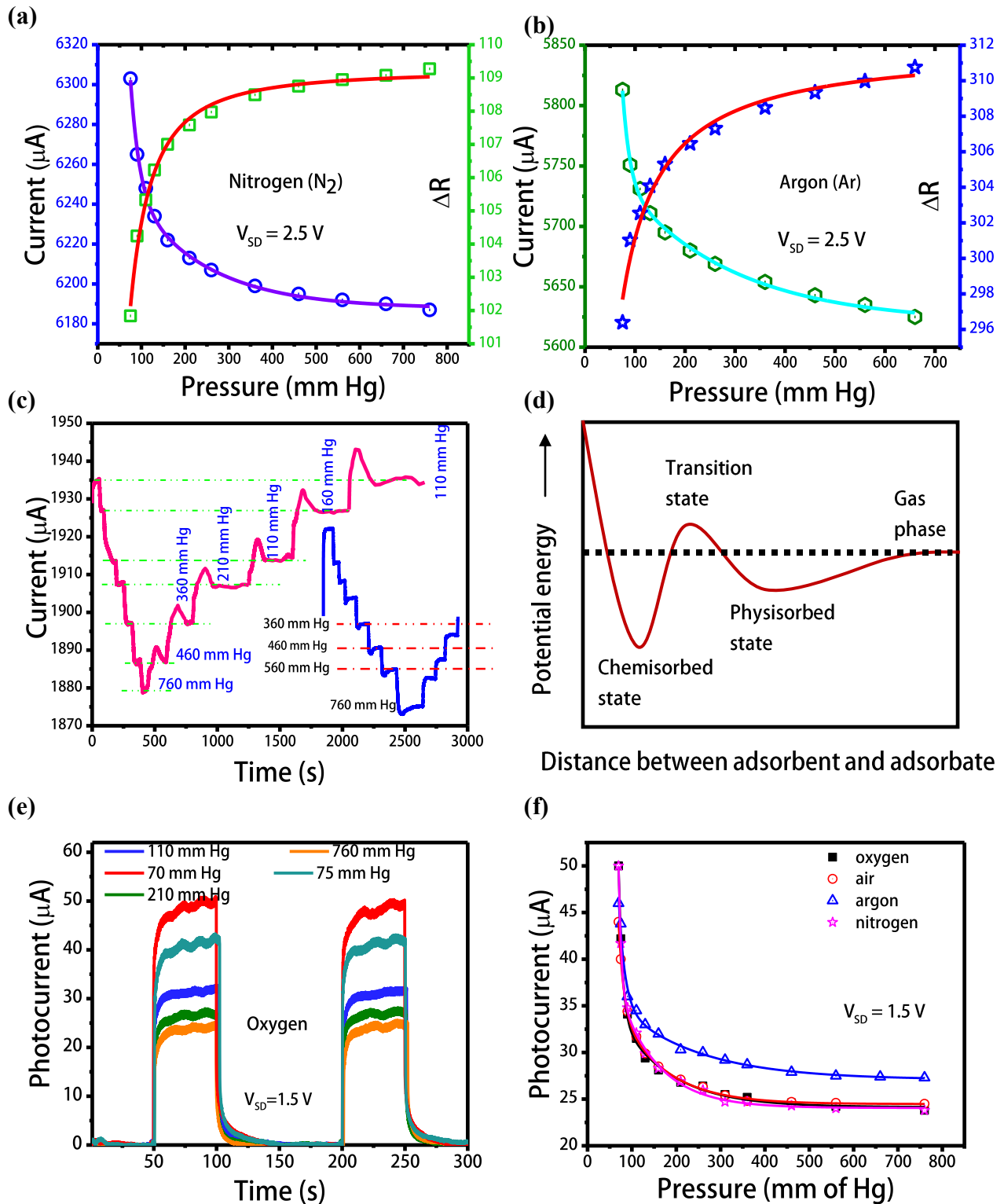
Figure 4: Current and resistance variation with gas (N_2, Ar) pressure (a),(b); (c) dark current vs. time at different pressure at 40° C in air (inset: at room temperature); (d) energy diagram of adsorption process; (e) temporal photoresponse at different pressure; (f) photocurrent variation with pressure.

$$\Delta \mathbf{R} = \frac{\alpha KP}{1+KP} \qquad \text{or} \qquad \Delta \mathbf{R} = \frac{\alpha KP^{1-m}}{1+KP^{1-m}},$$

where α, K, m are constants and P is the pressure of the gas. The first equation is well known Langmuir equation and the second equation is known as extended Langmuir (LangmuirEXT) equation and for m = 1 the equation takes the form of Langmuir equation. In case of Langmuir fit K value is proportional to equilibrium constant. Different fitting parameters have been listed in table 2.

Table 2: ΔR vs. P fitting parameters

Gas	Langmuir Isotherm			LangmuirEXT Isotherm			
	α	K	R^2_{adj}	α	m	K	R^2_{adj}
Nitrogen	110.2	0.185	0.97	109.2	-0.6	0.014	0.991
Oxygen	27.7	0.048	0.925	26.5	-1.0	5.46*E-4	0.999
Argon	312.0	0.277	0.977	311.1	-0.2	0.124	0.976
Air	60.4	0.05	0.967	67.78	0.54	0.350	0.990

LangmuirEXT fit possibly can also suggest how gas molecules adsorb on adsorbent surface. For oxygen, nitrogen and argon m values obtained are approximately -1, -0.5 and 0. Being a single atom molecule argon (Ar) can adsorb at a single position on the π-electron cloud of rGO which results in proportional increase in resistance with increase in pressure. It is well known that oxygen is physiosorbed creating 2 partial bonds from 2 oxygen atoms (oxygen is bimolecular) on the opposite C-atom of hexagonal ring of graphene which results in slight increase in O-O bond

length (Yan et al., 2012). Interestingly, ΔR follows a P^2 variation which could be due to each oxygen molecule forms two co-ordination to the π-electron cloud of graphene/reduced graphene oxide sheets. For N_2, m = 0.5 can be realized from 50-50 formation single and double coordination, which could be possible if energy difference between single and double coordination is very less (Rani et al., 2013, Rani et al., 2014, Zhechkov et al., 2006). A schematic of adsorbed gas molecule on hexagonal ring C-atoms of graphene sheet has been shown in schematic 1. In depth analysis of these data requires more research and comparison with other experimental and theoretical data which are out of scope of this current article.
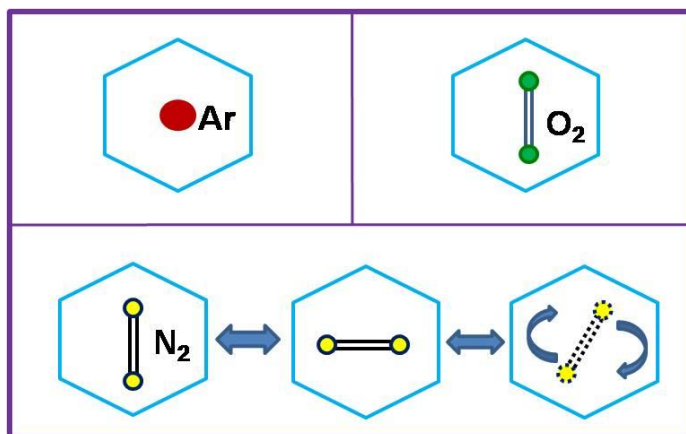
Schematic 1: Molecular arrangements of adsorbed gas molecule on hexagonal ring of graphene/rGO.

In order to explain the effect of gas adsorption on electrical property, we have carried out Hall measurements which indicates that rGO is n-type in nature. Both the adsorbed oxygen (O_2) and nitrogen (N_2) attract electron cloud from graphene sheet leading to decreased charge carriers in n-type rGO which leads to increased resistance (Yan et al., 2012, Rani et al., 2013, Rani et al., 2014). The increase in resistance is also observed for adsorbed argon. Graphene sheets are known to adsorb noble gases and adsorption has been attributed to the interaction between

fluctuating dipoles and evaluated by Lennard Jones model (Price, 1974, Rybolt and Pierotti, 1979). Adsorption of argon deforms the planar structure and thus, inhibits electron flow through graphene sheet, which ultimately leads to an increased resistance (Kysilka et al., 2011). Intercalation of molecules between rGO sheets can also lead to increased resistance (Papamatthaiou et al., 2017). In the presence of a nitrogen-ammonia mixture, the resistance initially increases and then decreases. The decrease in resistance is believed to be due to electron donating effect of ammonia which can increase carrier concentration of n-type rGO (figure S8 c) (Feng et al., 2016, Liu et al., 2011a).

In order to check the reproducibility of dark current after increasing the pressure, we have started decreasing pressure in steps and found that at room temperature (24°C) there is a lag in dark current (figure 4c inset). We have checked the dark current variation with pressure at 40°C and have found that dark current variation is reproducible (figure 4c). Slight fluctuation in dark current is due to fluctuation in PID controller which occurs when vacuum pump is turned on. This kind of behavior can be explained by energy diagram of free and adsorbed gas molecules (figure 4d). At room temperature and higher pressure the gas molecules gets adsorbed on rGO. As the physiosorbed molecules are stabilized by some amount of energy, a complete reversible transformation may not happen at room temperature. However, at an elevated temperature (40°C), this stabilization is easy to overcome and a complete reversible transformation happens. Overall, rGO behaves as a potential pressure sensor. One drawback associated with rGO is that at elevated temperature amount of adsorption decreases and saturation occurs even at lower pressure.

We have also shown how photocurrent varies with pressure (figure 4e and S9 a,b,c). Photocurrent decreases and saturates with increasing gas pressure. Photocurrent follows a bi-

exponential behavior, fast decrease followed by slow saturation (figure 4f). Repeated measurements show photocurrent decrease behavior is same for air, oxygen and nitrogen, while photocurrent saturates early in case of novel gas argon. Photocurrent decreases possibly due to increasing resistance upon absorption and also adsorbed sites can affect recombination of photogenerated electron and holes.

4. Conclusion:

In conclusion, rGO has been synthesized by a green hydrothermal synthesis route and characterized by various characterization techniques. rGO exhibits excellent broadband photodetection property, responsivity of the detector in NIR region is ~0.7A.W^{-1} and EQE in UV region is 120% which are much better than many previous reports. As the resistance of the device follows a well-defined exponential behavior with variation of temperature, we can exploit this property for temperature sensing purpose. Sensitivity of the rGO as temperature sensor is greater than commercial Pt-based temperature sensor. Thus, our device can act as a low cost and efficient photodetector and temperature sensor. Pressure dependent ΔR is similar to its gas adsorption behavior and photocurrent variation characteristic with pressure has also been reported.

Compliance with ethical standards

Conflict of Interest - The authors declare that they have no conflict of interest.

Appendix. Supplementary Information

Supplementary data are available in supplementary information file.

References:

AFZALI, P., ABDI, Y. & ARZI, E. 2014. Gated graphene/titanium dioxide-based photodetector. *Journal of Nanoparticle Research,* 16**,** 2659.

ALTUNTAS, H., OZGIT-AKGUN, C., DONMEZ, I. & BIYIKLI, N. 2015. Current transport mechanisms in plasma-enhanced atomic layer deposited AlN thin films. *Journal of Applied Physics,* 117**,** 155101.

ARORA, N., MARTINS, D., RUGGERIO, D., TOUSIMIS, E., SWISTEL, A. J., OSBORNE, M. P. & SIMMONS, R. M. 2008. Effectiveness of a noninvasive digital infrared thermal imaging system in the detection of breast cancer. *The American Journal of Surgery,* 196**,** 523-526.

BURGARD, D. A., DALTON, T. R., BISHOP, G. A., STARKEY, J. R. & STEDMAN, D. H. 2006. Nitrogen dioxide, sulfur dioxide, and ammonia detector for remote sensing of vehicle emissions. *Review of Scientific Instruments,* 77**,** 014101.

CHANG, H., SUN, Z., SAITO, M., YUAN, Q., ZHANG, H., LI, J., WANG, Z., FUJITA, T., DING, F., ZHENG, Z., YAN, F., WU, H., CHEN, M. & IKUHARA, Y. 2013. Regulating Infrared Photoresponses in Reduced Graphene Oxide Phototransistors by Defect and Atomic Structure Control. *ACS Nano,* 7**,** 6310-6320.

CHITARA, B., KRUPANIDHI, S. & RAO, C. 2011. Solution processed reduced graphene oxide ultraviolet detector. *Applied Physics Letters,* 99**,** 113114.

CHOWDHURY, F. A., MOCHIDA, T., OTSUKI, J. & ALAM, M. S. 2014. Thermally reduced solution-processed graphene oxide thin film: An efficient infrared photodetector. *Chemical Physics Letters,* 593**,** 198-203.

DEGNER, M., DAMASCHKE, N., EWALD, H., O'KEEFFE, S. & LEWIS, E. UV LED-based fiber coupled optical sensor for detection of ozone in the ppm and ppb range. Sensors, 2009 IEEE, 2009. IEEE, 95-99.

DIAS, S. & KRUPANIDHI, S. 2016. Solution processed Cu2SnS3 thin films for visible and infrared photodetector applications. *AIP Advances,* 6**,** 025217.

DIAS, S., KUMAWAT, K., BISWAS, S. & KRUPANIDHI, S. B. 2017a. Solvothermal synthesis of Cu2SnS3 quantum dots and their application in near-infrared photodetectors. *Inorganic Chemistry,* 56**,** 2198-2203.

DIAS, S., KUMAWAT, K. L., BISWAS, S. & KRUPANIDHI, S. 2017b. Heat-up synthesis of Cu 2 SnS 3 quantum dots for near infrared photodetection. *RSC Advances,* 7**,** 23301-23308.

FENG, Q., LI, X., WANG, J. & GASKOV, A. M. 2016. Reduced graphene oxide (rGO) encapsulated Co3O4 composite nanofibers for highly selective ammonia sensors. *Sensors and Actuators B: Chemical,* 222**,** 864-870.

FURCHI, M., URICH, A., POSPISCHIL, A., LILLEY, G., UNTERRAINER, K., DETZ, H., KLANG, P., ANDREWS, A. M., SCHRENK, W., STRASSER, G. & MUELLER, T. 2012. Microcavity-Integrated Graphene Photodetector. *Nano Letters,* 12**,** 2773-2777.

GAN, X., SHIUE, R.-J., GAO, Y., MERIC, I., HEINZ, T. F., SHEPARD, K., HONE, J., ASSEFA, S. & ENGLUND, D. 2013. Chip-integrated ultrafast graphene photodetector with high responsivity. *Nature Photonics,* 7**,** 883-887.

GEORGE, P. A., STRAIT, J., DAWLATY, J., SHIVARAMAN, S., CHANDRASHEKHAR, M., RANA, F. & SPENCER, M. G. 2008. Ultrafast Optical-Pump Terahertz-Probe Spectroscopy of the Carrier Relaxation and Recombination Dynamics in Epitaxial Graphene. *Nano Letters,* 8**,** 4248-4251.

GOWDA, P., SAKORIKAR, T., REDDY, S. K., FERRY, D. B. & MISRA, A. 2014. Defect-Induced Enhancement and Quenching Control of Photocurrent in Few-Layer Graphene Photodetectors. *ACS Applied Materials & Interfaces,* 6**,** 7485-7490.

GROBE, L., PARASKEVOPOULOS, A., HILT, J., SCHULZ, D., LASSAK, F., HARTLIEB, F., KOTTKE, C., JUNGNICKEL, V. & LANGER, K.-D. 2013. High-speed visible light communication systems. *IEEE Communications Magazine,* 51**,** 60-66.

HUMMERS JR, W. S. & OFFEMAN, R. E. 1958. Preparation of graphitic oxide. *Journal of the American Chemical Society,* 80**,** 1339-1339.

ITO, Y., ZHANG, W., LI, J., CHANG, H., LIU, P., FUJITA, T., TAN, Y., YAN, F. & CHEN, M. 2016. 3D Bicontinuous Nanoporous Reduced Graphene Oxide for Highly Sensitive Photodetectors. *Advanced Functional Materials,* 26**,** 1271-1277.

JUNG, K., KIM, Y., IM, H., KIM, H. & PARK, B. 2011. Leakage transport in the high-resistance state of a resistive-switching NbOx thin film prepared by pulsed laser deposition. *J. Korean Phys. Soc,* 59**,** 2778-2781.

KHAN, M. A., NANDA, K. K. & KRUPANIDHI, S. B. 2017a. Mechanistic view on efficient photodetection by solvothermally reduced graphene oxide. *Journal of Materials Science: Materials in Electronics,* 28**,** 14818-14826.

KHAN, M. A., NANDA, K. K. & KRUPANIDHI, S. B. 2017b. Reduced graphene oxide film based highly responsive infrared detector. *Materials Research Express,* 4**,** 085603.

KIND, H., YAN, H., MESSER, B., LAW, M. & YANG, P. 2002. Nanowire ultraviolet photodetectors and optical switches. *Advanced materials,* 14**,** 158.

KUMAR, A., HUSALE, S., SRIVASTAVA, A., DUTTA, P. & DHAR, A. 2014. Cu–Ni nanoparticle-decorated graphene based photodetector. *Nanoscale,* 6**,** 8192-8198.

KUMAR, P. & THANGARAJ, R. 2008. Analysis of bias field influenced recombination processes in narrow gap Sb2Se3 films. *Journal of Physics: Condensed Matter,* 20**,** 095213.

KYSILKA, J. I., RUBES, M., GRAJCIAR, L. S., NACHTIGALL, P. & BLUDSKÝ, O. 2011. Accurate description of argon and water adsorption on surfaces of graphene-based carbon allotropes. *The Journal of Physical Chemistry A,* 115**,** 11387-11393.

LI, D., MUELLER, M. B., GILJE, S., KANER, R. B. & WALLACE, G. G. 2008. Processable aqueous dispersions of graphene nanosheets. *Nature nanotechnology,* 3**,** 101-105.

LIU, H., LIU, Y. & ZHU, D. 2011a. Chemical doping of graphene. *Journal of Materials Chemistry,* 21**,** 3335-3345.

LIU, Y., CHENG, R., LIAO, L., ZHOU, H., BAI, J., LIU, G., LIU, L., HUANG, Y. & DUAN, X. 2011b. Plasmon resonance enhanced multicolour photodetection by graphene. *Nat Commun,* 2**,** 579.

MALLAMPATI, B., NAIR, S., RUDA, H. & PHILIPOSE, U. 2015. Role of surface in high photoconductive gain measured in ZnO nanowire-based photodetector. *Journal of Nanoparticle Research,* 17**,** 176.

MUCHHARLA, B., NARAYANAN, T., BALAKRISHNAN, K., AJAYAN, P. M. & TALAPATRA, S. 2014. Temperature dependent electrical transport of disordered reduced graphene oxide. *2D Materials,* 1**,** 011008.

MUKHOKOSI, E. P., KRUPANIDHI, S. B. & NANDA, K. K. 2018. An Extrinsic Approach Toward Achieving Fast Response and Self-Powered Photodetector. *physica status solidi (a)*.

NAIR, R., BLAKE, P., GRIGORENKO, A., NOVOSELOV, K., BOOTH, T., STAUBER, T., PERES, N. & GEIM, A. 2008. Fine structure constant defines visual transparency of graphene. *Science,* 320**,** 1308-1308.

PAPAMATTHAIOU, S., ARGYROPOULOS, D.-P., MASURKAR, A., CAVALLARI, M., FARMAKIS, F., KYMISSIS, I. & GEORGOULAS, N. 2017. Permanent water swelling effect in low temperature thermally reduced graphene oxide. *Applied Physics Letters,* 110**,** 252106.

PARIKSHIT, S., SAMPATH KUMAR, P., VADALI, V. S. S. & SUSHMEE, B. 2016. Graphene-based wearable temperature sensor and infrared photodetector on a flexible polyimide substrate. *Flexible and Printed Electronics,* 1**,** 025006.

PRICE, G. L. 1974. Potential energies of adsorbed rare gases on graphite. *Surface Science,* 46**,** 697-702.

RANI, B., JINDAL, V. & DHARAMVIR, K. Interaction of nitrogen molecule with graphene. AIP Conference Proceedings, 2013. AIP, 300-301.

RANI, B., JINDAL, V. & DHARAMVIR, K. Adsorption configurations of two nitrogen atoms on graphene. AIP Conference Proceedings, 2014. AIP, 450-452.

RYBOLT, T. R. & PIEROTTI, R. A. 1979. Rare gas–graphite interaction potentials. *The Journal of Chemical Physics,* 70**,** 4413-4419.

SENAPATI, S. & NANDA, K. K. 2017. Ultrahigh-sensitive optical temperature sensing based on quasi-thermalized green emissions from Er: ZnO. *Physical Chemistry Chemical Physics,* 19**,** 2346-2352.

TSUTSUMI, K., YAMASHITA, A. & OHJI, H. The experimental study of high TCR Pt thin films for thermal sensors. Sensors, 2002. Proceedings of IEEE, 2002. IEEE, 1002-1005.

VON ARX, M., PAUL, O. & BALTES, H. 1997. Test structures to measure the Seebeck coefficient of CMOS IC polysilicon. *IEEE transactions on semiconductor manufacturing,* 10**,** 201-208.

XIA, F., MUELLER, T., LIN, Y.-M., VALDES-GARCIA, A. & AVOURIS, P. 2009. Ultrafast graphene photodetector. *Nature nanotechnology,* 4**,** 839-843.

YAN, H., XU, B., SHI, S. & OUYANG, C. 2012. First-principles study of the oxygen adsorption and dissociation on graphene and nitrogen doped graphene for Li-air batteries. *Journal of Applied Physics,* 112**,** 104316.

ZHANG, B. Y., LIU, T., MENG, B., LI, X., LIANG, G., HU, X. & WANG, Q. J. 2013. Broadband high photoresponse from pure monolayer graphene photodetector. *Nat Commun,* 4**,** 1811.

ZHANG, Q., JIE, J., DIAO, S., SHAO, Z., ZHANG, Q., WANG, L., DENG, W., HU, W., XIA, H. & YUAN, X. 2015. Solution-processed graphene quantum dot deep-UV photodetectors. *ACS nano,* 9**,** 1561-1570.

ZHECHKOV, L., HEINE, T. & SEIFERT, G. 2006. Physisorption of N2 on graphene platelets: An ab initio study. *International Journal of Quantum Chemistry,* 106**,** 1375-1382.